



Article

Modulations of the South China Sea Ocean Circulation by the Summer Monsoon Intraseasonal Oscillation Inferred from Satellite Observations

Zhiyuan Hu ¹, Keiwei Lyu ^{1,*} and Jianyu Hu ^{1,2}

¹ State Key Laboratory of Marine Environmental Science, Center for Marine Meteorology and Climate Change, College of Ocean and Earth Sciences, Xiamen University, Xiamen 361102, China; zyhu19@xmu.edu.cn (Z.H.); hujy@xmu.edu.cn (J.H.)

² Southern Marine Science and Engineering Guangdong Laboratory (Zhuhai), Zhuhai 519082, China

* Correspondence: keweilyu@xmu.edu.cn

Abstract: The South China Sea (SCS) displays remarkable responses and feedback to the summer monsoon intraseasonal oscillation (ISO). This study investigates how the SCS summer ocean circulation responds to the monsoon ISO based on weekly satellite data. In summer, the largest amplitudes for intraseasonal (30–90 days) sea surface height variations in the SCS occur around the northeastward offshore current off southeast Vietnam between a north–south eddy dipole. Our results show that such strong intraseasonal sea surface height variations are mainly caused by the alternate enhancement of the two eddies of the eddy dipole. Specifically, in response to the intraseasonal intensification of southwesterly winds, the northern cyclonic eddy of the eddy dipole strengthens within 1–2 weeks, and its southern boundary tends to be more southerly. Afterwards, as the wind-driven southern anticyclonic gyre spins up, the southern anticyclonic eddy gradually intensifies and expands its northern boundary northward, while the northern cyclonic eddy weakens and retreats northward. Besides the local wind forcing, westward propagations of the eastern boundary-originated sea surface height anomalies, which exhibit latitude-dependent features that are consistent with the linear Rossby wave theory, play an important role in ocean dynamical adjustments to the monsoon ISO, especially in the southern SCS. Case studies further confirm our findings and indicate that understanding this wind-driven process makes the ocean more predictable on short-term timescales.



Citation: Hu, Z.; Lyu, K.; Hu, J. Modulations of the South China Sea Ocean Circulation by the Summer Monsoon Intraseasonal Oscillation Inferred from Satellite Observations. *Remote Sens.* **2024**, *16*, 1195. <https://doi.org/10.3390/rs16071195>

Academic Editor: Kaoru Ichikawa

Received: 1 March 2024

Revised: 22 March 2024

Accepted: 24 March 2024

Published: 29 March 2024



Copyright: © 2024 by the authors. Licensee MDPI, Basel, Switzerland. This article is an open access article distributed under the terms and conditions of the Creative Commons Attribution (CC BY) license (<https://creativecommons.org/licenses/by/4.0/>).

Keywords: South China Sea; intraseasonal oscillation; ocean response; Rossby wave; offshore current; eddy dipole

1. Introduction

As part of the Asian monsoon system, the sea surface wind over the South China Sea (SCS) shows pronounced seasonal variability, which in turn drives upper-ocean seasonal circulation in the SCS [1–3]. In summer, under the prevailing southwesterly winds (Figure 1a), the SCS basin-scale ocean circulation is dominated by a double-gyre structure (Figure 1b). It consists of a northeastward offshore current off southeast Vietnam between around 10°N and 14°N, an energetic anticyclonic gyre in the southern SCS, and a weaker cyclonic gyre to the north [4–6]. The net effect of the inertial process of the wind-driven southern (northern) gyre is to advect negative (positive) vorticity northward (southward) via the northward (southward) western boundary current [7,8]. Therefore, there is often an eddy dipole structure off central Vietnam with an anticyclonic eddy (AE) south of the offshore current and a cyclonic eddy (CE) north of it. Gan and Qu [5] indicated that around the offshore current, the nonlinear vorticity advection is mainly balanced by the bottom pressure torque, i.e., the effects of shelf topography. Upwelling also takes place off the south Vietnam coast due to the alongshore wind and the strong local positive wind stress

curl (WSC), while the offshore current helps to advect the cold coastal water into the deep basin and contributes substantially to the deformation of the upwelling area [9–12].

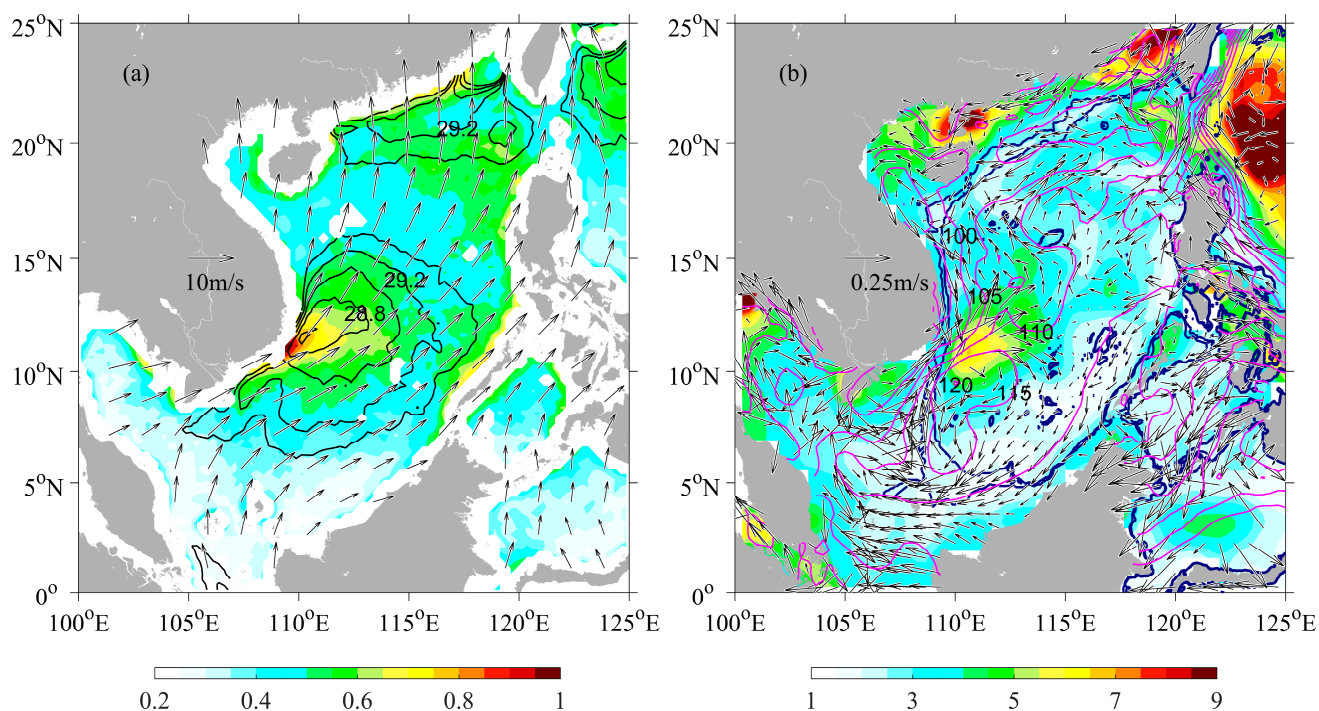


Figure 1. (a) Multi-year averaged summer sea surface wind (vectors), SST (contours, °C) and standard deviation of the 30–90-day filtered SST anomalies (color shading, °C) for June–September from 2000 to 2009. (b) Multi-year averaged summer geostrophic currents (vectors), ADT (magenta contours, cm), and standard deviation of the 30–90-day filtered SSH anomalies (color shading, cm) for June–September from 2000 to 2009. The isobaths of 100 m and 200 m (blue lines) are shown in (b).

The SCS summer monsoon exhibits prominent intraseasonal oscillations (ISOs) characterized by the northward-migrating monsoon trough–ridge system in the lower troposphere (Mao and Chan [13]; Zheng and Huang [14]). Intraseasonal signals of the sea surface temperature (SST) [15], the mixed-layer and upper-ocean temperatures [16], the latent heat flux [17], the sea surface height (SSH) [18], the western boundary current [19], the cross-slope flow [20], the subsurface thermocline [21,22], the deep ocean temperature [23], the energy budget [24], and the deep current [25] in the SCS have been widely reported on. As for the summer upwelling area in the western SCS (Figure 1a), the related SST cooling and phytoplankton bloom often experience several intraseasonal events each summer [26–30]. It should be noted that the oceanic intraseasonal signals are not just passive responses to the atmospheric forcing. Roxy and Tanimoto [31] highlighted the role of the SST in modulating the SCS summer monsoon ISO through the ocean-to-atmosphere feedback near the sea surface.

However, how the SCS summer ocean circulation responds to the monsoon ISO and evolves on intraseasonal timescales are still unclear. Xie et al. [28] pointed out that the SCS summer double-gyre ocean circulation strengthens in 2–3 weeks in response to the intraseasonal wind intensification via a Rossby wave adjustment. Wang et al. [32] suggested that both the cyclonic gyre in the northern SCS and the anticyclonic gyre in the southern SCS could be enhanced during the westerly phase of the Madden–Julian Oscillation (MJO), but with a much longer lag of ~40 days. To what extent the monsoon ISO could modulate the SCS summer ocean circulation is also unclear. Jan et al. [33] observed the ocean velocity ISOs in the central SCS during the summer monsoon season using mooring current measurements. Using satellite SSH data, they further indicated that Rossby waves with an SLA > 0.2 m propagating from the Pacific through the Sulu Sea into

the SCS could contribute to the velocity ISOs in the central SCS. This study aims to clarify how the SCS summer ocean circulation responds to the summer monsoon ISO. We argue that in response to the summer monsoon ISO, the two eddies of the eddy dipole in the western SCS strengthen alternately rather than simultaneously as suggested in previous studies.

The remainder of this paper is organized as follows. Section 2 introduces the data and methods used in this study. Section 3 presents the main results, including the dominant mode of intraseasonal SSH variations in the southern SCS (Section 3.1) and propagating features of the intraseasonal SSH signals (Section 3.2). Two case studies showing the evolutionary patterns of the SST, SSH, and velocity anomalies are also used to verify that the eddy dipole and ocean currents in the western SCS are indeed modulated by the summer monsoon ISO and, consequently, evolve in the way we suggest in this study (Section 3.3). The summary and discussions are given in Section 4.

2. Data and Methodology

2.1. Data

In this study, we analyzed the Quick Scatterometer (QuikSCAT) sea surface wind observations (Ricciardulli et al. [34]) and the Tropical Rainfall Measuring Microwave Imager (TMI) SST observations (Wentz et al. [35]) provided by Remote Sensing Systems (<http://www.remss.com> (accessed on 15 and 20 February 2017)), with a 0.25° by 0.25° resolution. The QuikSCAT was launched in June 1999 and operated until November 2009. The QuikScat data underwent a final reprocessing using the improved Ku-band Geophysical Model Function (GMF) after the instrument stopped functioning (Ricciardulli et al. [34]). The GMF was used to derive the wind speed and direction at a height of 10 m over ice-free oceans from backscattered scatterometer signals. The TMI was one of the instruments carried by the Tropical Rainfall Measuring Mission (TRMM), which was launched in November 1997. TMI is a multi-channel, dual-polarized, conical scanning passive microwave radiometer designed to measure rain rates over a wide swath under the TRMM satellite. In addition to rain rates, TMI also measured SST, sea surface wind speed, columnar water vapor, and cloud liquid water. The SSTs from TMI were the first satellite microwave SSTs available and have proven to be of great value to many areas of research (Wentz et al. [35]).

The multi-mission altimeter products, including the absolute dynamic topography (ADT), SSH anomalies, and geostrophic currents on a $1/3^\circ$ Mercator grid, were obtained from Archiving, Validation and Interpretation of Satellite Oceanographic data (AVISO, <http://www.aviso.oceanobs.com> (accessed on 10 February 2017)). The merge of multiple-satellite altimeter missions has demonstrated greater mesoscale mapping capability of SSH anomalies (Le Traon and Dibarboure [36]).

The weekly averaged satellite data over the period from July 1999 to November 2009 (i.e., the operation period of QuikSCAT) were analyzed. Data gaps were filled using linear spatial and temporal interpolations. A 30–90-day Lanczos bandpass filter was applied to the data to extract intraseasonal signals. Such a period band is commonly used in ISO studies [15,17]. In the following analysis, we focused on the boreal summer, i.e., from June to September, when the SCS is mainly controlled by the summer monsoon and its northward-propagating ISO [13].

Following Cai et al. [37], we used seasonally gridded ocean temperature and salinity climatology data with a 1° by 1° horizontal resolution from the World Ocean Atlas 2009 (WOA09) to calculate the phase speed (c_1) of the first baroclinic gravity wave and the westward phase speed (C_{R1}) of the first baroclinic Rossby wave in the SCS by solving the linearized vertical eigenvalue problem. The WOA09 data were made available by the National Oceanographic Data Center (NODC; Locarnini et al. [38], Antonov et al. [39]; <https://iridl.ldeo.columbia.edu/SOURCES/.NOAA/.NODC/.WOA09/> (accessed on 20 February 2017)) of the National Oceanic and Atmospheric Administration (NOAA).

2.2. Methodology

A conventional empirical orthogonal function (EOF) analysis yields stationary spatial patterns and varying time series for each pattern, which means that an EOF spatial pattern will only change in magnitude while the spatial structure remains the same. This is not the case for a spatially propagating phenomenon. The complex EOF (CEOF) method was introduced to include both the spatial and temporal covariance information. The CEOF method involves a Hilbert transform of the original data; thus, a propagating signal can be represented by one CEOF mode rather than a combination of a quadrature pair of EOFs. CEOF analysis has been widely used to study the propagation features of the mesoscale ocean dynamics (e.g., [19,40,41]). In this study, the CEOF analysis is used to identify the dominant mode of summer intraseasonal SSH variations in the southern SCS and the related propagation features.

We used a lagged regression analysis to describe the spatial evolution of the atmosphere–ocean system over the SCS. Given the reference time series x_t , when the dependent variable y_t lags x_t by Δt , the linear regression equation can be solved using the least-square fitting: $y_{t+\Delta t} = ax_t + b + \delta_{t+\Delta t}$, where a is the slope and the regression coefficient at lag(Δt), b is the intercept, and $\delta_{t+\Delta t}$ is the residual. In this study, the reference time series x_t was used as the normalized time series for the dominant CEOF mode of June-to-September intraseasonal SSH anomalies in the southern SCS (shown in Figure 2). The dependent time series y_t refers to June-to-September intraseasonal anomalies for each individual variable (including sea surface wind, WSC, SST, and SSH) at each grid point in the SCS region. In this way, we were able to identify how various variables co-vary at different lags with the dominant mode of intraseasonal SSH variations in the southern SCS. Note that the linear regression as a mathematical approach explores linear relations between the two time series (or variables) but does not imply any cause–effect relationship between them. The statistical significance of regressions is assessed using the t -test: $t = r\sqrt{N_{edof}/(1-r^2)}$, in which r is the correlation coefficient between the two time series and the effective degree of freedom (N_{edof}) is estimated using the method of Bretherton et al. [42]: ($N_{edof} = N(1 - r_1r_2)/(1 + r_1r_2)$), where N is the sample size of the data and r_1 and r_2 are the lag-one autocorrelations for the two time series, respectively.

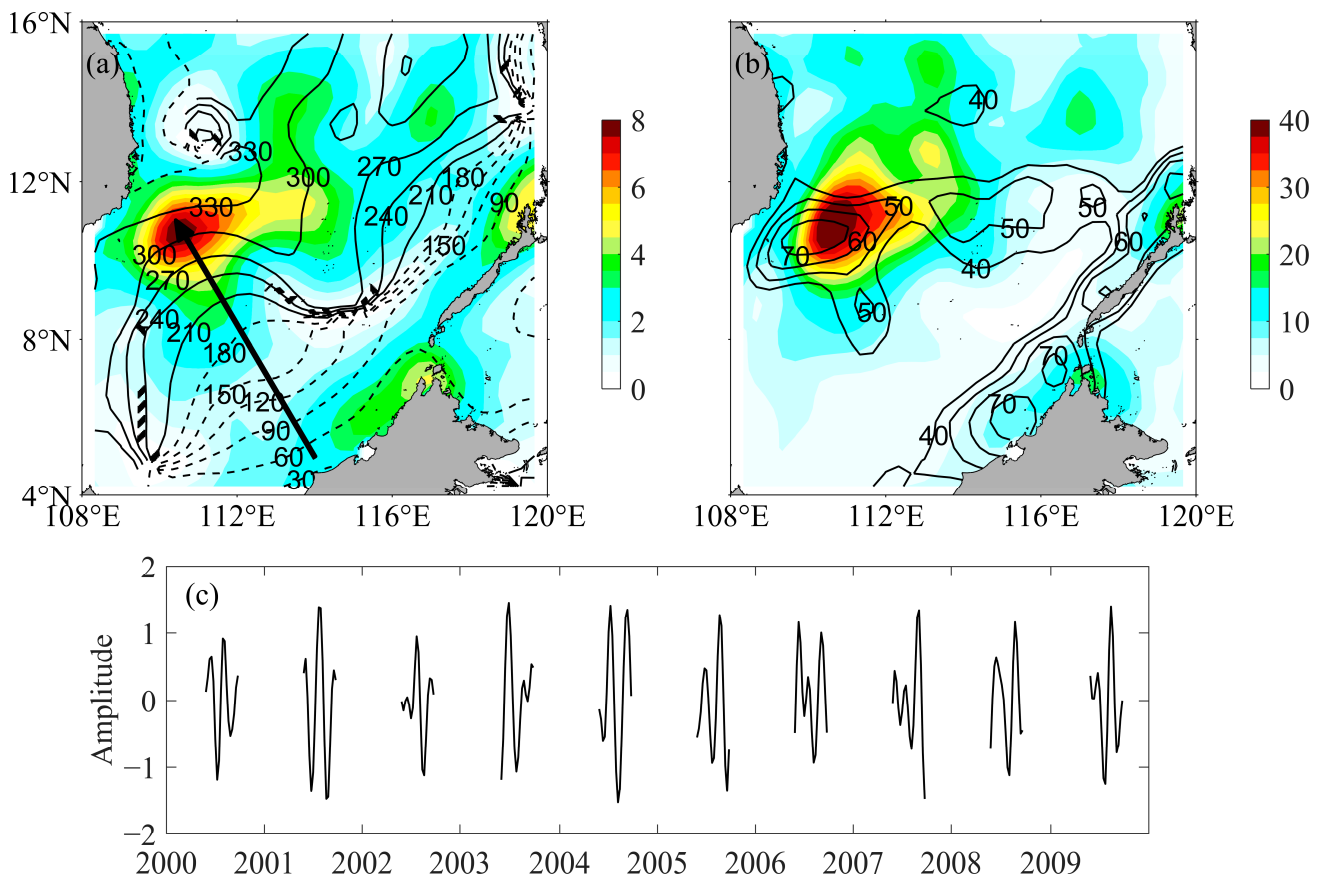


Figure 2. The CEOF1 of the 30–90-day filtered June-to-September SSH anomalies. (a) The CEOF1 spatial amplitude (color shading, cm) and phase (contours with the interval of 30°). The arrow indicates the direction of increased spatial phase, i.e., the propagating signal. (b) Local variance (color shading, cm^2) of the 30–90-day filtered June-to-September SSH anomalies and the percentage (contours, %) explained by the CEOF1. (c) The CEOF1 time series. Note that the intervals between individual years from October to the following May are added for illustrative purpose only as the CEOF analysis was applied to the synthesized June-to-September data with the temporal gaps between October and the following May ignored.

3. Results

3.1. The Dominant Mode of Intraseasonal SSH Variations in the Southern SCS: CEOF Analysis

The standard deviations of the 30–90-day filtered June-to-September SSH anomalies show a maximum center off southeast Vietnam around the northeastward offshore current (Figure 1b). In order to focus on this anomaly center and identify the dominant processes that lead to such strong SSH variations, we applied the CEOF analysis to the 30–90-day filtered June-to-September SSH anomalies in the southern SCS, specifically within a spatial domain of $4^\circ\text{--}16^\circ\text{N}$ and $108^\circ\text{--}120^\circ\text{E}$ (Figure 2). Specifically, we first derived the Hilbert transform of the full time series of the filtered SSH anomalies. The original time series at each grid point can be extended into a complex variable by adding its Hilbert transform as the imaginary part. We then excluded data from October to the following May. That means both the real and imaginary parts of the complex variable became time series of the synthesized June-to-September data, with the temporal gaps between October and the following May being ignored. Finally, a covariance matrix was constructed from this complex variable and processed like the standard EOF analysis. The first CEOF mode (CEOF1) explains 35.0% of the total variance and is well separated from modes 2 and 3, which explain 10.8% and 8.4% of the variance, respectively.

The CEOF1 spatial patterns show the largest amplitudes off southeast Vietnam roughly within 9° – 12° N and 109° – 113° E (Figure 2a), which can explain up to 70% of the local variance (Figure 2b). Such a high percentage suggests that CEOF1 captures the dominant mode for the strong intraseasonal SSH variations in this region. While the CEOF1 spatial amplitude represents the intensity of the propagating signals, the spatial phase increase also indicates the direction of signal propagation. Both the spatial amplitude and the explained variance percentage present high values near the eastern coasts of the SCS. The spatial phase distributions show lower values along the eastern coasts of the SCS. The spatial phase values increase gradually to the west, indicating a clear feature of westward propagations. The eastern boundary forcing could be the important origin of the westward propagating signals. Over the area of the southern anticyclonic gyre, the spatial phase field is fairly distinctive and characterized by a northwestward phase increase, i.e., the propagation of SSH anomalies. These propagating features will be detailed and explained in the next subsection.

A time series for CEOF1 was derived by multiplying the temporal amplitude by the sine of the temporal phase (Figure 2c). The autocorrelations of the CEOF1 time series show the largest negative correlations at a time lag of 4 weeks, indicating a typical period of 8 weeks (Figure 3a) which is consistent with the spectral analysis (Figure 4a). A wind index defined by Xie et al. [28] was calculated as the filtered wind speed anomalies averaged over 112° – 116° E and 9° – 13° N (see Figure 5c for the region). The maximum correlation of 0.70 occurs when the wind index leads the CEOF1 time series by one week (Figure 3b), which means that the CEOF1 represents the dynamical responses of the SCS to the intraseasonal wind variations of the summer monsoon.

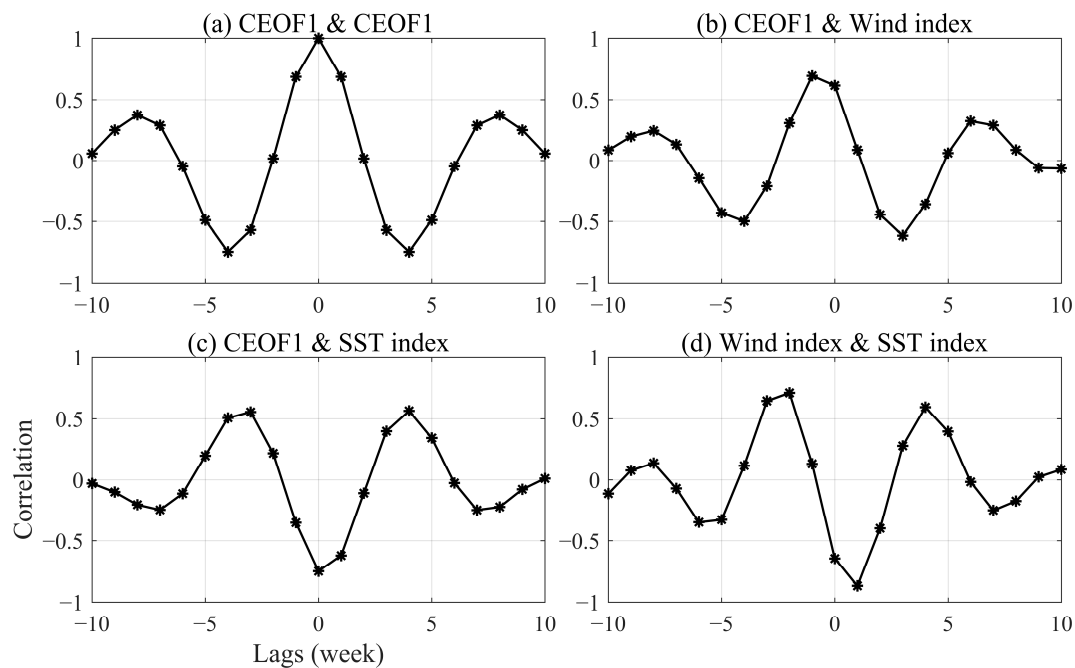


Figure 3. Lead-lag correlations of the CEOF1 time series with (a) the CEOF1 time series itself, (b) the wind index defined by Xie et al. [28], (c) the SST index defined by Isoguchi and Kawamura [26], (d) Lead-lag correlations between the wind index and the SST index. The former leads the latter for the positive lags.

The QuikSCAT sea surface winds were regressed onto the normalized CEOF1 time series at different time lags to show how the associated wind fields vary on intraseasonal timescales (Figure 5). While the CEOF1 time series is comprised of June-to-September time series from individual years (Figure 2c), the dependent time series for linear regression at lag time of Δt were derived from the full time series of sea surface winds by selecting

the corresponding time periods. For example, at lag 1, the time series from the second week of June to the first week of October in individual years were selected and then synthesized to be regressed onto the CEOF1 time series. Similarly, at lag -1 , the time series between the last week of May and the second last week of September in individual years were combined together for regression onto the CEOF1 time series. Note that the regressions are conducted in a larger spatial domain covering the SCS compared to the CEOF analysis to reveal the large-scale features. One week before the peak time of the CEOF1 time series (i.e., lag -1), the anomalous westerly or southwesterly winds prevail south of 15°N while the anomalous northeasterly winds appear over the northern SCS (Figure 5c). This anomalous cyclonic wind structure is also accompanied by negative WSC anomalies south of 10°N and positive WSC anomalies to the north. One week later, the anomalous southwesterly winds develop northward and cover most of the central SCS (Figure 5d). Thereafter, the anomalous southwesterly winds move further northward and eventually dissipate over the northern SCS (Figure 5e–h). Therefore, CEOF1 is associated with the northward development of anomalous wind structures, corresponding to the large-scale northward migration of suppressed or enhanced convection from the equator to the mid-latitudes for the summer monsoon ISO (e.g., Mao and Chan [13]).

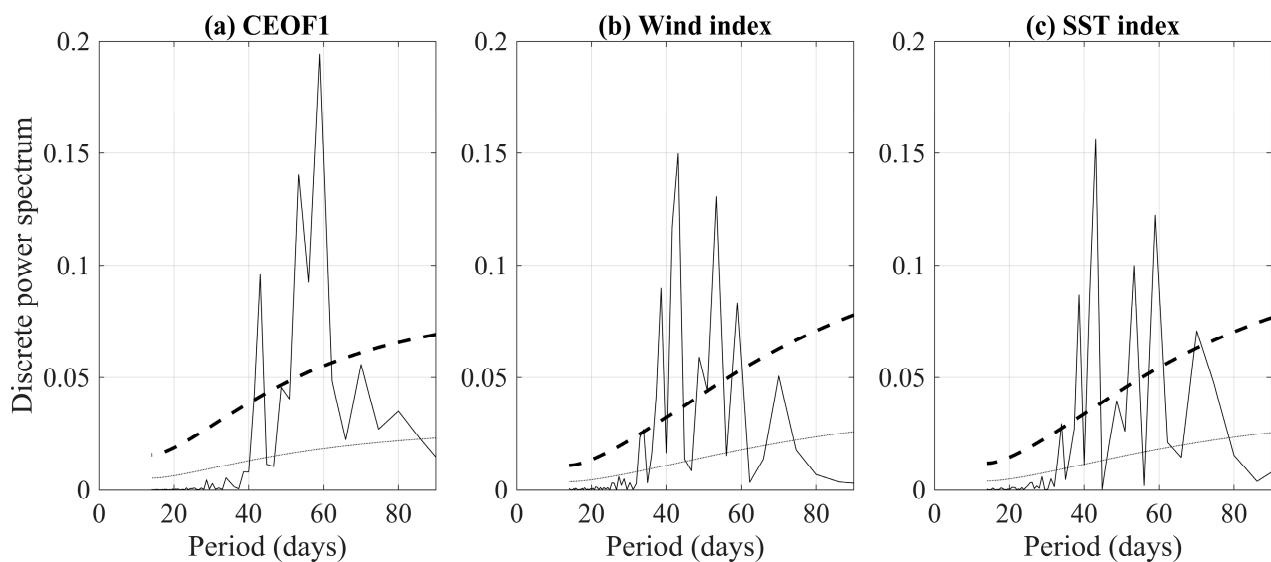


Figure 4. Power spectra of the normalized (a) CEOF1 time series, (b) wind index defined by Xie et al. [28], and (c) SST index defined by Isoguchi and Kawamura [26]. Dashed lines represent the 95% significant level. Dotted lines are for the red noise spectrum.

Gao and Zhou [15] showed that the summer intraseasonal SST variations also feature pronounced northward propagations across the SCS, which can be seen by regressing the SST data onto the CEOF1 time series (Figure 6). The SST cooling signals initially appear in the southern SCS, then intensify and develop northward following the anomalous southwesterly winds. The largest SST cooling occurs in the upwelling region off southeast Vietnam during the peak time of the CEOF1 time series (i.e., lag 0; Figure 6d). Isoguchi and Kawamura [26] defined an SST cooling index as the averaged SST anomalies over $109^{\circ}\text{--}114^{\circ}\text{E}$ and $9^{\circ}\text{--}12^{\circ}\text{N}$ (see Figure 6d for the region). Based on the lagged regression maps (Figure 6), the CEOF1 time series and the SST index reach the highest correlation of -0.75 without time lag (Figure 3c). That means about 56% (R-square) of the intraseasonal SST variance in the western SCS upwelling region can be explained by the SSH CEOF1. We also found that the wind index leads the SST index by one week with a correlation of -0.87 (Figure 3d), which is consistent with the strongest westerly wind anomalies at lag -1 (Figure 5c) and the maximum SST cooling at lag 0 (Figure 6d). Therefore, the lead–lag

relationships are consistent among the wind, SST, and SSH on intraseasonal timescales, as they are all closely related to the summer monsoon ISO.

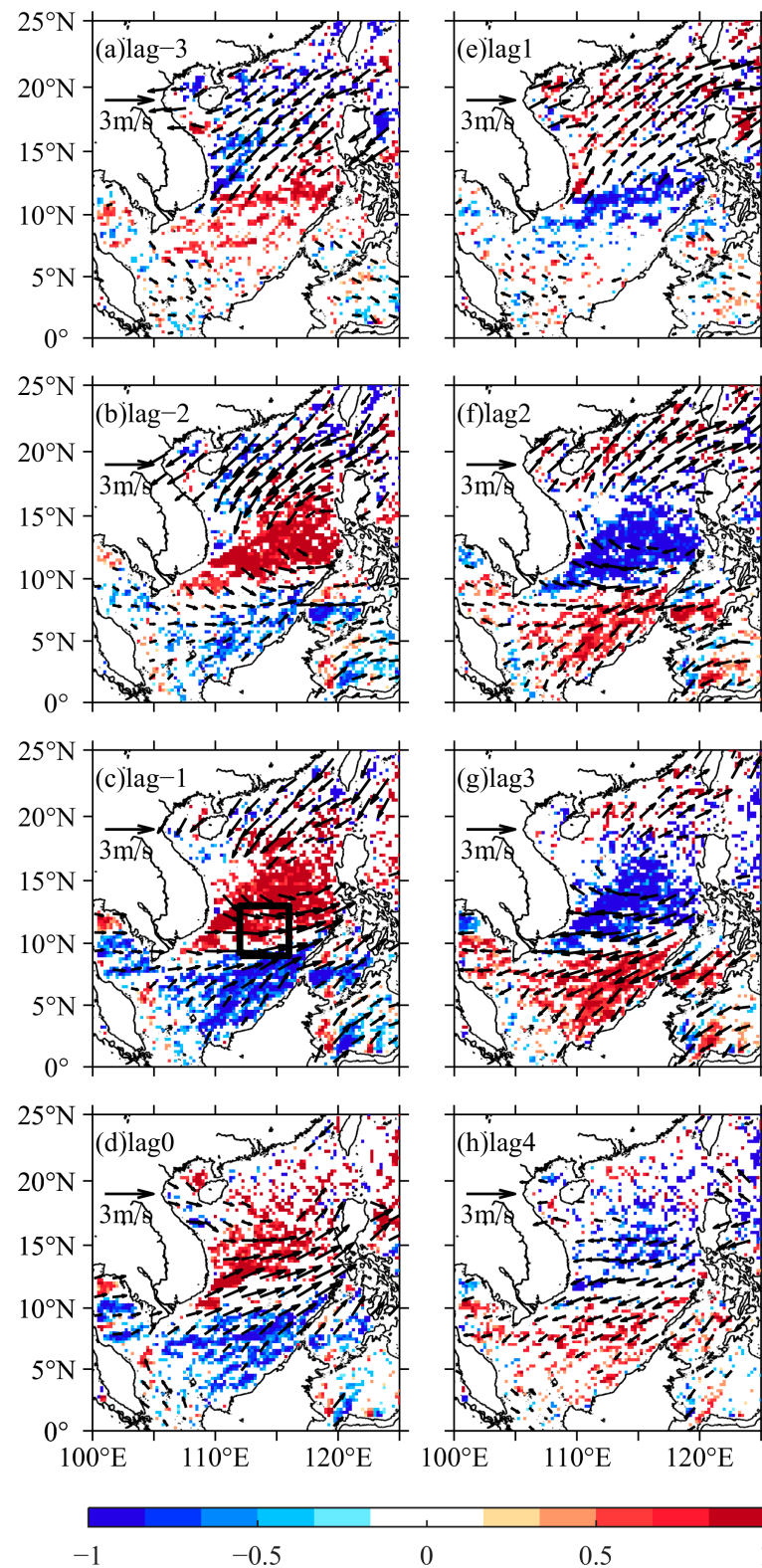


Figure 5. Lead-lag regression coefficients of the sea surface wind (vectors) and wind stress curl (WSC, 10^{-7} N m^{-3} , color shading) at each grid point against the normalized CEOF1 time series shown in Figure 2c. Only the regions with correlations exceeding the 90% significance level are plotted. The black square in (c) is the region that Xie et al. [28] calculated the wind index.

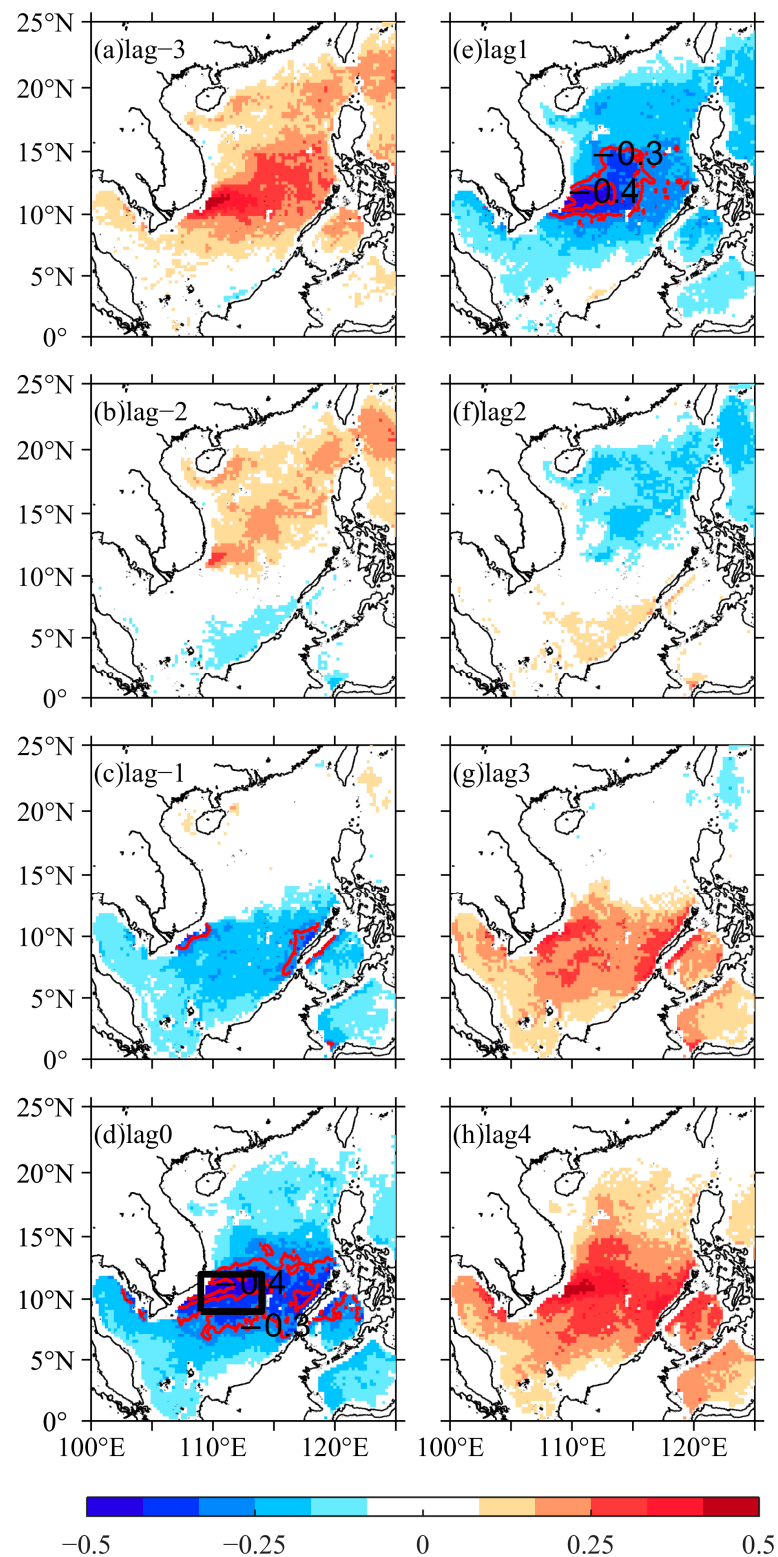


Figure 6. Lead-lag regression coefficients of the SST (°C, color shading) at each grid point against the normalized CEOF1 time series shown in Figure 2c. Only the regions with correlations exceeding the 90% significance level are plotted. The -0.3 and -0.4 °C isolines are also shown as contours. The black rectangular box in (d) is the region that Isoguchi and Kawamura [26] defined an SST cooling index.

While all the three indices show a significant spectral peak at the same period of nearly 8 weeks, there are also interesting differences between them (Figure 4). The power spectrum of the CEOF1 time series derived from the SSH shows a prominent 8-week spectral peak. In contrast, the wind index exhibits multiple spectral peaks on intraseasonal timescales, consistent with previous studies regarding the SCS summer monsoon ISO [13]. This contrast suggests that while wind forcing is an important driver for intraseasonal SSH variations, the ocean dynamical processes seem to set the timescale for ocean circulation adjustment in response to the wind forcing and thus determine the dominant frequency for SSH variations. Meanwhile, the 8-week spectral peak is relatively large for the SST index compared to the wind index, suggesting a role of ocean dynamics (indicated by the SSH) in SST variations in addition to direct forcing from the wind. In the next subsection, we will focus on propagation features of the intraseasonal SSH variations to identify how the SCS summer ocean circulation responds to the summer monsoon ISO.

It is important to note that the aliasing periods of M_2 and S_2 tidal constituents in the altimetry data are very close to 8 weeks [43]. Thus, it is likely that the tidal correction error might contribute to the identified dominant period of intraseasonal SSH variations, especially in shallow areas. However, we note that the largest SSH anomalies off southeast Vietnam, i.e., the focus of this study, are located in the deep basin (Figure 1b) and thus should be less affected by the tidal aliasing effect. Moreover, the dominant periods for intraseasonal SSH variations differ between seasons. We checked another CEOF1 time series for intraseasonal SSH variations in the southern SCS but for the winter season (October to March) [19]. Both winter CEOF1 time series and the wind index that represents the SCS winter monsoon ISO exhibit a spectral peak at a different period of 7 weeks. This seasonal contrast further supports the robustness of intraseasonal SSH variations.

3.2. Propagation Features of the Intraseasonal SSH Signals

We also regressed the SSH anomaly data onto the CEOF1 time series to reveal the associated space–time evolutions for intraseasonal SSH anomalies (Figure 7). Note that similar SSH evolutions can also be constructed from the CEOF1 mode itself. In response to the anomalous northeasterly winds in the northern SCS at lag -1 (Figure 5c), the positive SSH anomalies occur on the northern SCS shelf as a result of the inshore volume transport (Figure 7c). Such intraseasonal wind anomalies could temporally interrupt the coastal upwelling in the northern SCS, which has important ecological effects [44]. At the same time, the anomalous southwesterly winds in the southern SCS also drive positive SSH anomalies along the eastern coasts of the SCS (Figure 7c). Conversely, the nearly opposite-signed wind anomalies at lag 3 (Figure 5g), i.e., the weakening phase for the summer monsoon ISO, produce negative SSH anomalies near the northern and eastern coasts of the SCS (Figure 7g).

At lag 0, i.e., one week after the peak phase of the southwesterly winds, there is a center of negative SSH anomalies off southeast Vietnam which extends northeastward to the central basin (Figure 7d). Afterwards, these negative SSH anomalies are slightly displaced northward and nearly disappear at lag 3. Meanwhile, the eastern boundary-generated positive SSH anomalies gradually propagate westward at lag -1 , corresponding to the westward phase increase to the west of the eastern boundary (Figure 2a). The northward phase increase in the southern SCS (Figure 2a) also corresponds to the northward development of the positive SSH anomalies at lag -1 , which helps to form a northeasterly oriented region of positive SSH anomalies off southeast Vietnam at lag 4 (Figure 7h). Note that since the typical time period is ~ 8 weeks, the two patterns at lag 0 and lag 4 are nearly out of phase on intraseasonal timescales. Therefore, it seems that both the northward and eastward propagation processes contribute to the strong SSH variations off southeast Vietnam.

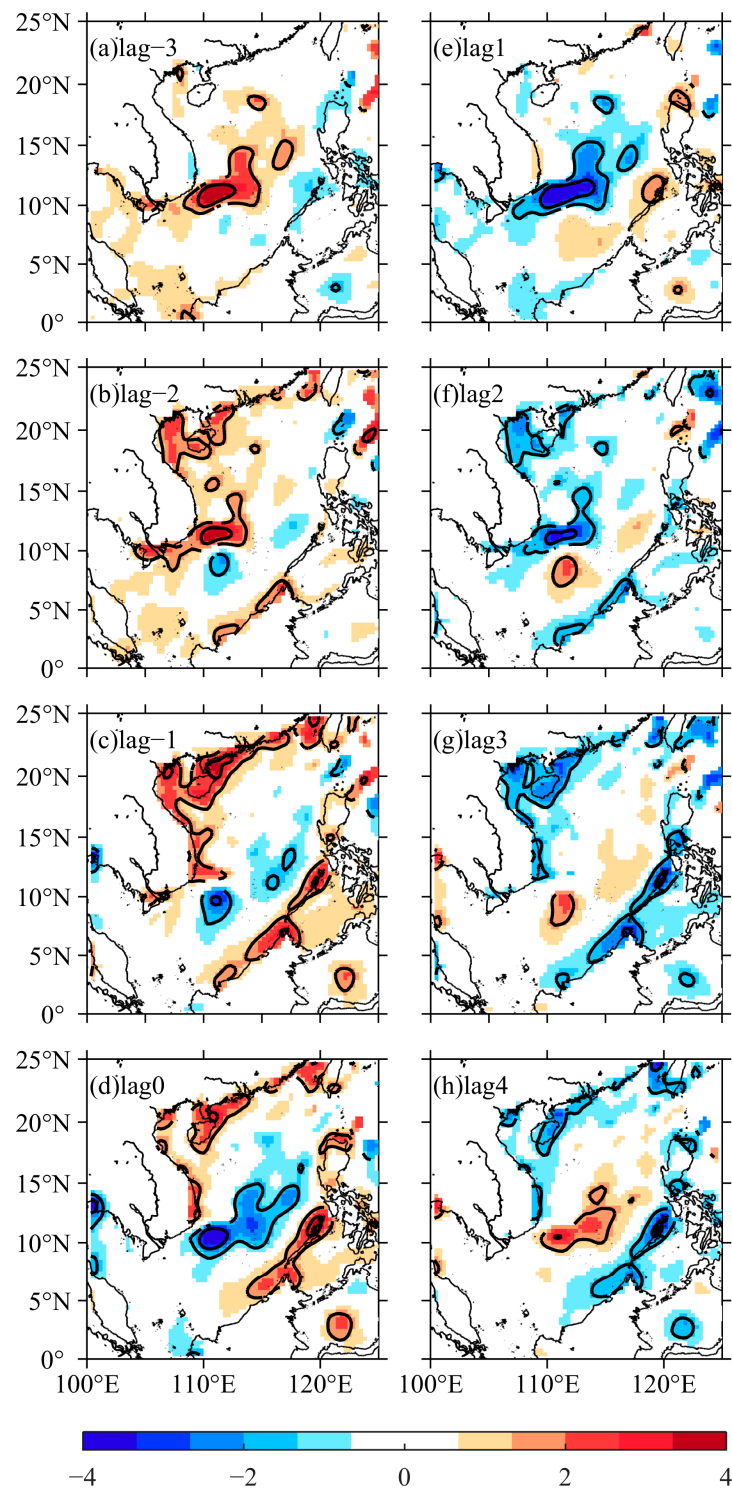


Figure 7. Lead–lag regression coefficients of the SSH (cm, color shading) at each grid point against the normalized CEOF1 time series shown in Figure 2c. Only the regions with correlations exceeding the 90% significance level are plotted. The ± 1.5 and ± 3 cm isolines are also shown as contours.

The westward propagations can be seen clearly from the time–longitude distributions of the regressed SSH anomalies (Figure 8). Alternate positive and negative SSH anomalies appear at the eastern boundary of the SCS and propagate westward. It is estimated that the phase speed of the westward propagation is about 35 cm s^{-1} along 7°N and 19 cm s^{-1} along 11°N . These values are fairly close to the westward phase speeds (C_{R1}) of the first

baroclinic Rossby wave at the corresponding latitudes (Figure 9a). Such consistency links the westward propagation signals to the Rossby waves excited at the eastern boundary of the SCS basin.

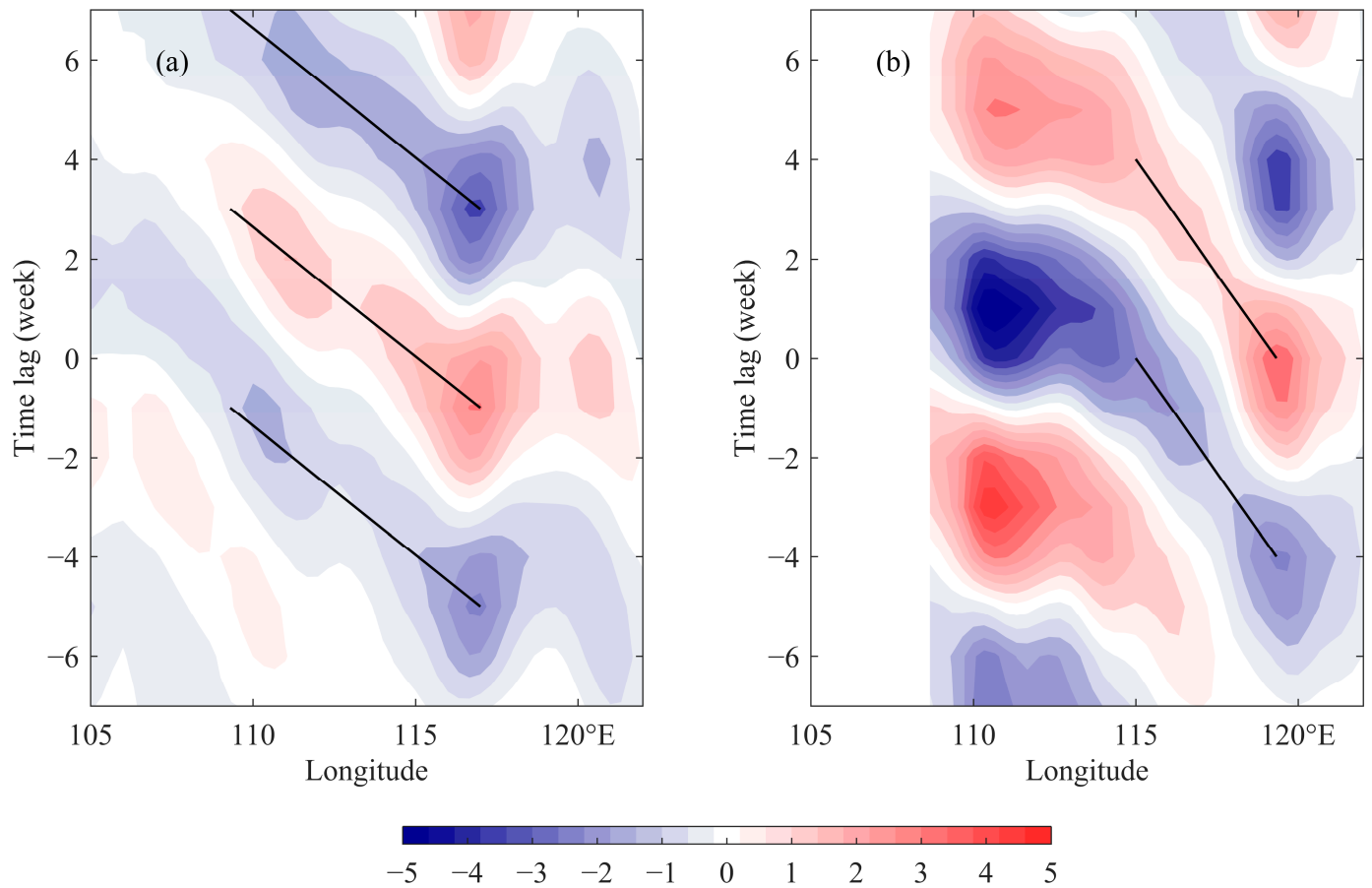


Figure 8. Time–longitude distributions of the regressed SSH anomalies (cm) along (a) 7°N and (b) 11°N. The solid lines in the figures indicate the propagation characteristics.

Xie et al. [28] identified the westward propagation of intraseasonal SSH anomalies with a speed of about 37 cm/s at 12°N, which was also attributed to the ocean Rossby wave. However, this propagation speed is much faster than the phase speed of the Rossby wave at this latitude, which is around 15–20 cm/s (Figure 9a). It should be noted that they estimated the westward propagation speed along a short zonal band between 110°E and 116°E, where the largest SSH anomalies exist. Our results also show that the westward propagation signals along 11°N seem to accelerate to the west of 115°E (Figure 8b). The faster propagation speed that they identified could involve the interaction between the offshore current and the planetary wave and thus should not be viewed as free Rossby waves.

We also noticed that the offshore westward phase increases are less coherent north of 13°N (Figure 2a), which means the westward propagation signals become weak. One explanation is the restriction of the critical period (T_c), which is defined as: $T_c = (4\pi f) / (\beta c_1)$, where c_1 is the phase speed of the first baroclinic gravity wave and β is the variation in the Coriolis parameter (f) with latitude. T_c represents the theoretical cut-off period of freely propagating baroclinic Rossby waves. The coastal signals with periods of $T > T_c$ radiate into the central SCS basin as Rossby waves, while the signals with $T < T_c$ remain coastally trapped. The T_c values in the SCS generally increase with latitude (Figure 9b), similar to the global distributions [45].

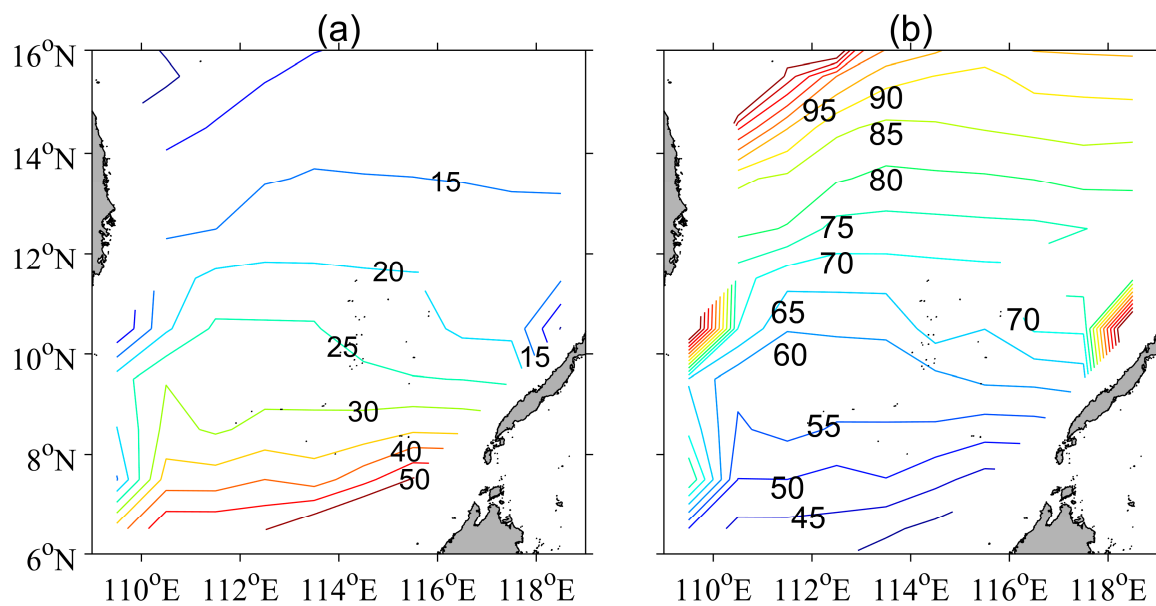


Figure 9. Distributions for (a) the westward phase speed C_{R1} (cm s^{-1}) of the first baroclinic Rossby wave, and (b) the critical period (days) in the southern SCS calculated from the WOA09 summer data. Only areas deeper than 200 m are plotted.

We also examined the meridional structures of the WSC and SSH anomaly, as shown in Figure 10. It appears that in the deep basin between 6°N and 13°N , the northward propagating positive (negative) WSC anomaly is closely followed by negative (positive) SSH anomaly with a lag of 2 weeks through the local Ekman pumping effect. However, a closer inspection reveals that around 11°N , the maximum SSH anomaly is located just south of the largest WSC anomaly. Clearly, the highly fluctuant SSH anomaly along the offshore current may not be viewed as a simple and direct response to the local WSC forcing or the remote influence of planetary waves alone. As shown in Figure 7, the largest intraseasonal SSH anomaly is located around the offshore current southeast of Vietnam. We suggest the alternate enhancement of the eddy pair and the resulting meridional migration of their border as the direct driver, which will be further demonstrated in the next subsection through two case studies.

We acknowledge that the SSH propagations discussed above cover areas where the amplitudes of intraseasonal SSH variations are rather small (Figure 2). This might cause concern that the identified propagations, albeit largely consistent with the linear Rossby wave theory, might be pseudo-signals connecting independent areas. To further verify the spatial phase relationship for intraseasonal SSH anomalies as shown above, we directly calculated the covariance between the 30–90-day filtered June-to-September SSH anomalies and the normalized SSH anomalies on the east coast. The covariance amplitude shows the offshore continuity of the SSH signals within intraseasonal frequency bands along different paths (Figure 11). Along the northwestward phase-increase direction in the southern SCS (shown as the arrow in Figure 2a), the SSH anomalies behave as one complete wavelength with less attenuation. This feature represents a phase difference of about 360° and confirms that the northwestward phase increase in the southern SCS identified by CEOF1 is reliable. Along 11°N , the offshore structure is rather continuous, but a large proportion of the energy is still coastally trapped. Since T_c is 65–70 days around 11°N (Figure 9b) and the typical time period is 8 weeks, the role of Rossby wave propagations at this latitude is potentially weakened. At a higher latitude (15°N), with a T_c value of about 85–90 days, the sea level signal rapidly attenuates away from the eastern coasts, indicating that the intraseasonal SSH signal at this latitude is mainly coastally trapped. This kind of coastally trapped phenomenon was once observed via current mooring near the western coast of India at the same latitude [46].

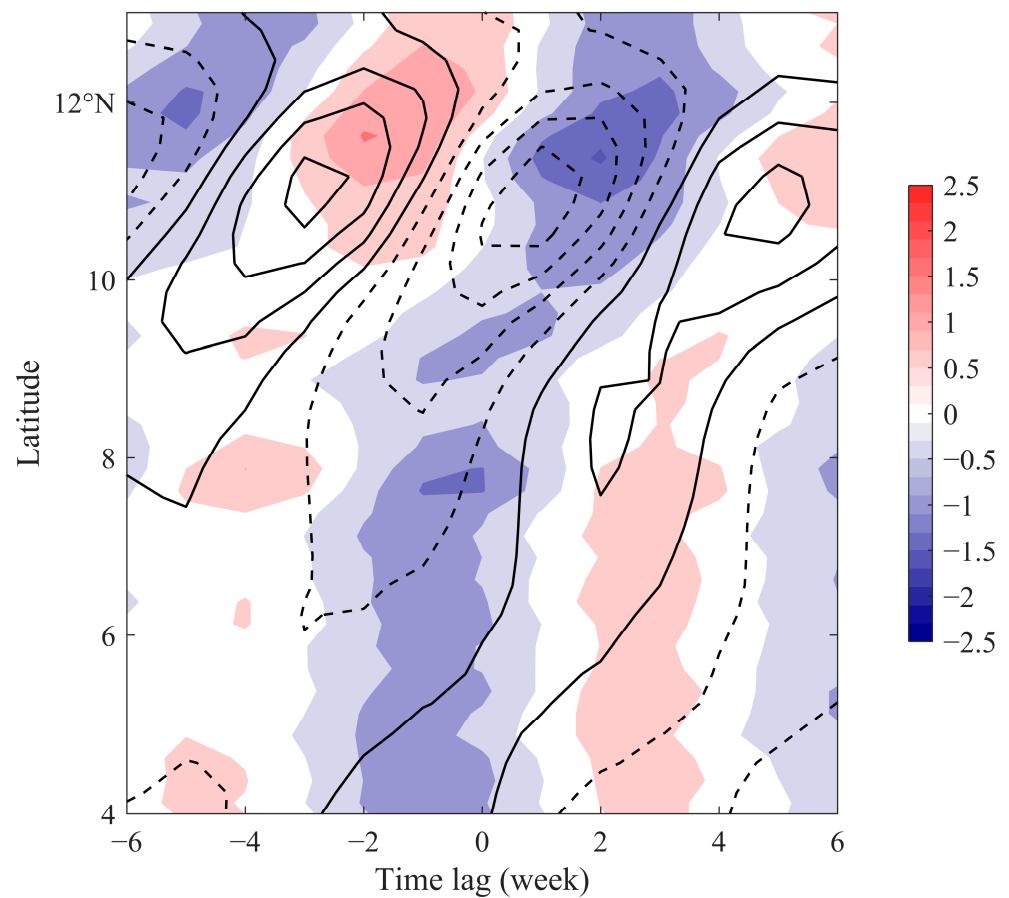


Figure 10. Time–latitude distributions of the regressed wind stress curl (WSC, 10^{-7} N m^{-3} , color shading) and SSH anomalies (cm, contours) averaged between 110°E and 113°E . Solid (dashed) lines mean positive (negative) SSH anomalies.

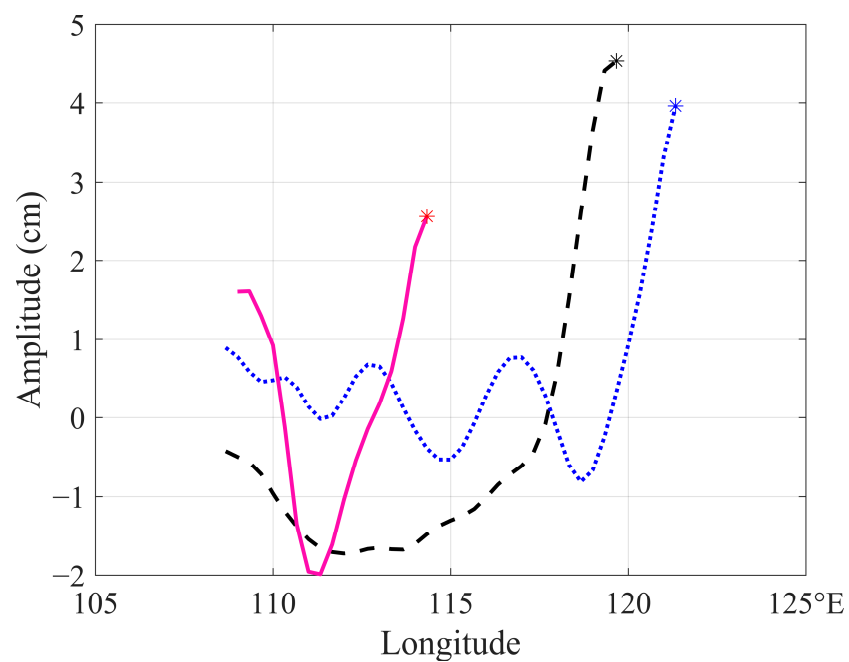


Figure 11. The covariance between the 30–90-day filtered June-to-September SSH anomalies and the normalized anomalies at the east coast (indicated by the asterisk in the right endpoint) along 15°N (blue dotted line), 11°N (black dashed line), and the arrow shown in Figure 2a (red solid line).

3.3. Case Studies

One may still wonder whether the summer SCS ocean circulation can be significantly modulated by the intraseasonal wind variability. One typical intraseasonal event was selected to address this question, with a special focus on the evolution of cold water, the eddy pair, and the offshore current in the western SCS (Figure 12). The summer of 2002 was chosen because the double gyre circulation was stronger than that in other years [47].

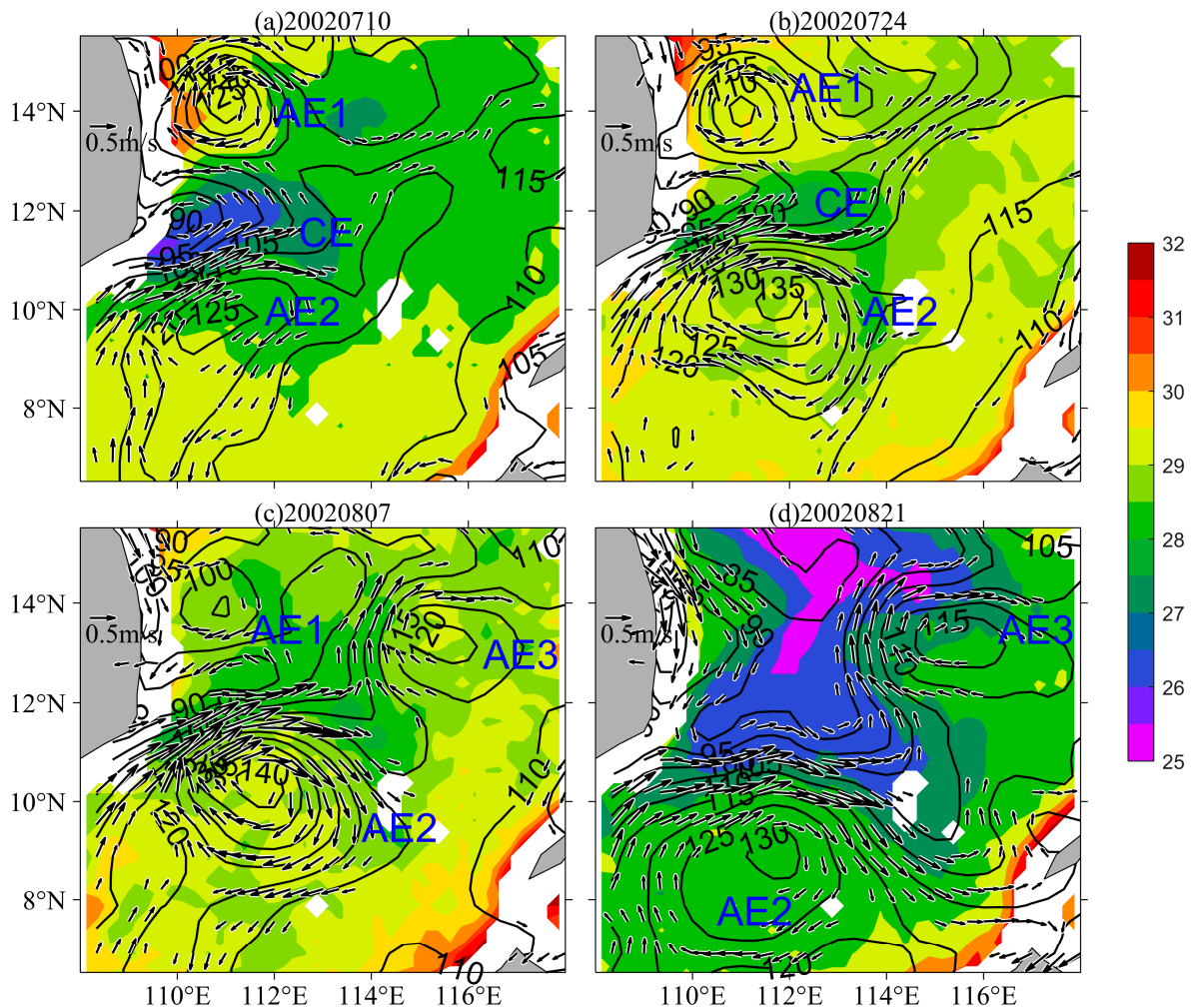


Figure 12. Weekly averaged maps of SST ($^{\circ}\text{C}$, color shading), ADT (cm, contours with 5 cm interval) and geostrophic current (vector) greater than 20 cm s^{-1} centered on (a) 10 July, (b) 24 July, (c) 7 August and (d) 21 August 2002.

This case clearly shows that the intraseasonal variation of the eddy pair is out of phase. The alternating development of the eddy pair, which can be explained by the wind-related mechanisms discussed above, directly leads to the meridional migration of their border and the high SSH anomaly between the eddies.

On 10 July 2002, there were three coexisting eddies located next to the western boundary. A CE with a lower central ADT value of 90 cm and a lower SST was sandwiched by two AEs (AE1 and AE2) both with higher central ADT values of 125 cm (Figure 12a). Two weeks later, both the area and the central value of AE2 increased greatly and the offshore current intensified and shifted northward; CE seemed to be squeezed and decayed (Figure 12b). On 7 August, AE2 and the related geostrophic current reached their peak intensity, with the central ADT reaching 140 cm, while CE almost disappeared. Meanwhile, another AE (AE3) appeared at around 116°E and 13°N (Figure 12c). Hu et al. [48] presented the three-dimensional structure of CE in early September 2007 using in situ current

and hydrographic measurements, also indicating that the CE was significantly influenced by AE2.

We tried to link the evolution of the eddies to the regressed maps of the SSH. One week after the burst of southwesterly winds, CE developed on 10 July (Figure 12a). For the next four weeks, the enhancement of AE2 and the formation of AE3 (Figure 12b,c) were in good agreement with the positive SSH anomaly that occurred in the same regions. On 21 August, the central ADT values of AE2 and AE3 decreased by 10 cm and 5 cm, respectively, and the offshore current migrated southward (Figure 12d). This corresponding relationship boosts our confidence in forecasting the life cycle of the eddy pair based on the atmospheric forcing.

The other spatial patterns for the intraseasonal evolution in the summer of 2004 are shown in Figure 13. From the early summer to 23 June 2004 (Figure 13a), CE and the cold-water region developed in response to southwesterly winds; to the north of CE, AE1 was reduced over time. Thereafter, with the enhancement of the southern gyre, AE2 formed and pushed the CE to the north (around 12°N), and the eddy pair structure was gradually established. On 21 July (Figure 13b), AE2 and the offshore current reached their first peak, while AE1 nearly disappeared. As shown in Figure 13c, CE reached its greatest intensity and AE2 was suppressed on 25 August. Meanwhile, the offshore current shifted southward. Similar to the situation in Figure 13b, AE2 reached its peak phase again on 15 September (Figure 13d), which was also accompanied by a northward shift in the offshore current.

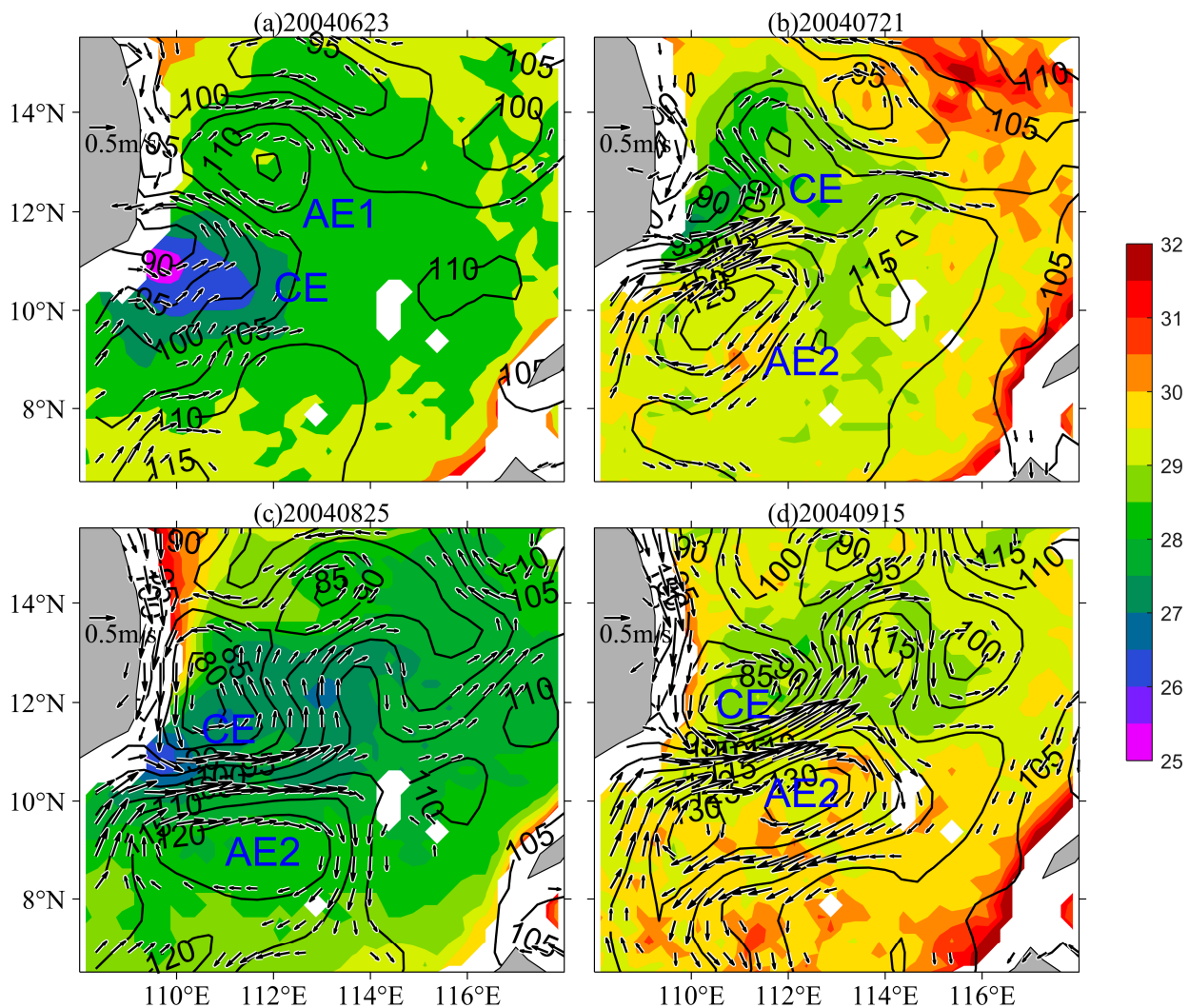


Figure 13. Same as in Figure 12 but on (a) 23 June, (b) 21 July, (c) 25 August, and (d) 15 September, 2004.

4. Summary and Discussion

The boreal summer ISOs of the atmospheric and oceanic parameters in the SCS were investigated based on weekly satellite data, including QuikSCAT sea surface wind data, TMI SST data, and SSH data provided by the AVISO. The focus has been put on the evolutionary patterns and mechanisms of the ocean dynamical response, which has important implications for better understanding and improving the short-term predictability of an ocean system with mesoscale phenomena. The observed westward propagations of intraseasonal SSH anomalies that evidently originate from the eastern boundary exhibit remarkable meridional dependence, which can be interpreted using linear wave theory. The observed phase speeds with larger values at lower latitudes agree well with the westward phase speed for the first baroclinic Rossby wave. The offshore propagations at higher latitudes are restrained by the critical period. These features confirm that the baroclinic Rossby wave dynamics are fundamental to the dynamical adjustments of the large-scale ocean circulation in response to the atmospheric ISO.

Our results can be summarized into the following processes: (1) In response to the intraseasonal intensification of southwesterly winds, the northern CE of the eddy dipole in the western SCS strengthens locally, while the positive SSH anomalies induced by the anomalous southwesterly winds along the eastern boundary of the SCS excite downwelling Rossby waves, which freely propagate westward. (2) At lower latitudes, they are fast enough to reinforce the response directly forced by the negative WSC anomaly in the interior of the southern anticyclonic gyre. (3) This interaction effectively leads to the enhancement of the southern anticyclonic gyre and its associated current. (4) The enhanced northward western boundary current and offshore current tend to advect and accumulate the negative vorticity (or low planetary potential vorticity) to the northern border, eventually resulting in the local maxima of the positive SSH anomaly along the offshore current. During this process, the southern AE of the eddy pair intensifies and develops northward progressively whilst the CE weakens and retreats northward. The next half cycle evolves in the same way but with an anomaly of opposite sign. In short, the background ocean circulation acts as a self-regulating system to shape the most outstanding dynamical responses to the atmospheric ISO forcing. Case studies in the summers of 2002 and 2004 were used to demonstrate the linkage between the variation of the eddy pair and the atmospheric ISO.

The baroclinic instability of the mean flow is also critical to this high-anomaly area. Although the background field in summer indeed favors the occurrence of baroclinic instability in this region, our results indicate that, modulated by the atmospheric ISO, the short-term fluctuations of the eddy pair and the offshore current path could play a more important role, at least contributing to the predictable part. Numerical experiments with the intraseasonal signals of winds being removed could be designed to isolate the intrinsic instability of the mean flow and the modulation of the intraseasonally varying wind.

So far, we have clarified how the SCS responds to the atmospheric ISO. In light of the significant air–sea interaction in the SCS on intraseasonal timescales [31], the proportions of different contributions to the upper-ocean heat budget, including surface heat fluxes, horizontal advection, and subsurface processes, need to be further determined. High-resolution numerical simulation is required to make quantitative estimates at different stages of the atmospheric ISO, as in the work conducted by Vinayachandran et al. [49] for the Bay of Bengal, another region highly influenced by the Asian summer monsoon ISO. Within this modeling framework, the details of the dynamical interaction between the mean and fluctuating flows can also be determined.

Author Contributions: Conceptualization, K.L. and J.H.; funding, K.L. and J.H.; methodology, K.L.; writing—original draft preparation, Z.H. and K.L.; writing—review and editing, K.L. and J.H. All authors have read and agreed to the published version of the manuscript.

Funding: This study was jointly supported by the National Natural Science Foundation of China (91958203) and the National Key R&D Program of China (2023YFF0806500).

Data Availability Statement: The datasets for the research are publicly available. The Quick Scatterometer (QuikSCAT) sea surface wind and the Tropical Rainfall Measuring Microwave Imager (TMI) SST observations are provided by the Remote Sensing Systems (<http://www.remss.com> (accessed on 15 and 20 February 2017)). The multi-mission altimeter products, including the absolute dynamic topography (ADT), SSH anomalies, and geostrophic currents, were obtained from the Archiving, Validation and Interpretation of Satellite Oceanographic data (AVISO, <http://www.aviso.oceanobs.com> (accessed on 10 February 2017)).

Acknowledgments: We appreciate all the constructive comments from the Academic Editor and three anonymous reviewers that have improved early version of the manuscript. We also appreciate Jianjie Feng for the help of making some figures.

Conflicts of Interest: The authors declare no conflicts of interest. The funders had no role in the design of the study; in the collection, analyses, or interpretation of data; in the writing of the manuscript, or in the decision to publish the results.

References

1. Hu, J.; Kawamura, H.; Hong, H.; Qi, Y. A review on the currents in the South China Sea: Seasonal circulation, South China Sea warm current and Kuroshio intrusion. *J. Oceanogr.* **2000**, *56*, 607–624. [[CrossRef](#)]
2. Liu, Q.; Jia, Y.; Liu, P.; Wang, Q.; Chu, P.C. Seasonal and intraseasonal thermocline variability in the central South China Sea. *Geophys. Res. Lett.* **2001**, *28*, 4467–4470. [[CrossRef](#)]
3. Wang, D.; Wang, W.; Shi, P.; Guo, P.; Gan, Z. Establishment and adjustment of monsoon-driven circulation in the South China Sea. *Sci. China Ser. D* **2003**, *46*, 173–191. [[CrossRef](#)]
4. Cai, S.; Long, X.; Wang, S. A model study of the summer Southeast Vietnam offshore Current in the southern South China Sea. *Cont. Shelf Res.* **2007**, *27*, 2357–2372. [[CrossRef](#)]
5. Gan, J.; Qu, T. Coastal jet separation and associated flow variability in the Southwest South China Sea. *Deep Sea Res. Part I* **2008**, *55*, 1–19. [[CrossRef](#)]
6. Liu, Q.; Kaneko, A.; Su, J. Recent progress in studies of the South China Sea circulation. *J. Oceanogr.* **2008**, *64*, 753–762. [[CrossRef](#)]
7. Wang, G.; Chen, D.; Su, J. Generation and life cycle of the dipole in the South China Sea summer circulation. *J. Geophys. Res.* **2006**, *111*, C06002. [[CrossRef](#)]
8. Bayler, E.J.; Liu, Z. Basin-scale wind-forced dynamics of the seasonal southern South China Sea gyre. *J. Geophys. Res.* **2008**, *113*, C07014. [[CrossRef](#)]
9. Kuo, N.J.; Zheng, Q.; Ho, C.R. Satellite observation of upwelling along the western coast of the South China Sea. *Remote Sens. Environ.* **2000**, *74*, 463–470. [[CrossRef](#)]
10. Xie, S.-P.; Xie, Q.; Wang, D.; Liu, W.T. Summer upwelling in the South China Sea and its role in regional climate variations. *J. Geophys. Res.* **2003**, *108*, 3261. [[CrossRef](#)]
11. Zhuang, W.; Wang, D.; Hu, J.; Ni, W. Response of the cold water mass in the western South China Sea to the wind stress curl associated with the summer monsoon. *Acta Oceanol. Sin.* **2006**, *25*, 1–13.
12. Hu, J.; Wang, X.H. Progress on upwelling studies in the China seas. *Rev. Geophys.* **2016**, *54*, 653–673. [[CrossRef](#)]
13. Mao, J.; Chan, J.C.L. Intraseasonal variability of the South China Sea summer monsoon. *J. Clim.* **2005**, *18*, 2388–2402. [[CrossRef](#)]
14. Zheng, B.; Huang, Y.Y. Mechanisms of northward-propagating intraseasonal oscillation over the South China Sea during the pre-monsoon period. *J. Clim.* **2019**, *32*, 3297–3311. [[CrossRef](#)]
15. Gao, R.; Zhou, F. Monsoonal characteristics revealed by intraseasonal variability of sea surface temperature (SST) in the South China Sea (SCS). *Geophys. Res. Lett.* **2002**, *29*, 1222. [[CrossRef](#)]
16. Jia, W.; Sun, J.; Zhang, W.; Wang, H. The effect of boreal summer intraseasonal oscillation on mixed layer and upper ocean temperature over the South China Sea. *J. Ocean. Univ. China* **2023**, *22*, 285–296. [[CrossRef](#)]
17. Zeng, L.; Wang, D. Intraseasonal variability of latent-heat flux in the South China Sea. *Theor. Appl. Climatol.* **2009**, *97*, 53–64. [[CrossRef](#)]
18. Zhuang, W.; Xie, S.-P.; Wang, D.; Taguchi, B.; Aiki, H.; Sasaki, H. Intraseasonal variability in sea surface height over the South China Sea. *J. Geophys. Res.* **2010**, *115*, C04010. [[CrossRef](#)]
19. Lyu, K.W.; Yang, X.Y.; Zheng, Q.; Wang, D.; Hu, J. Intraseasonal variability of the winter western boundary current in the South China Sea using satellite data and mooring observations. *IEEE J. Sel. Top. Appl. Earth Obs. Remote Sens.* **2016**, *9*, 5079–5088. [[CrossRef](#)]
20. Wang, Q.; Zhou, W.D.; Zeng, L.; Chen, J.; He, Y.K.; Wang, D.X. Intraseasonal variability of cross-slope flow in the northern South China Sea. *J. Phys. Oceanogr.* **2020**, *50*, 2071–2084. [[CrossRef](#)]
21. Liu, Z.; Yang, H.; Liu, Q. Regional dynamics of seasonal variability in the South China Sea. *J. Phys. Oceanogr.* **2001**, *31*, 272–284. [[CrossRef](#)]

22. Zeng, L.; Wang, D.; Du, Y.; Shi, P. Mesoscale structure of the central detected by SCSMEX Buoy and Argo float. *Chin. J. Oceanol. Limnol.* **2010**, *28*, 1102–1111. [[CrossRef](#)]
23. Mao, J.; Wang, M. Intraseasonal responses of sea surface and deep oceanic temperature anomalies in the northern Indian Ocean–western Pacific to the 30–60-day boreal summer atmospheric intraseasonal oscillation. *Clim. Dyn.* **2019**, *53*, 4539–4552. [[CrossRef](#)]
24. Quan, Q.; Liu, Z.; Yang, Y.; Cai, Z.; Zhang, H.; Liu, X. Characterization of intraseasonal fluctuations in the abyssal south china sea: An insight into the energy pathway. *Prog. Oceanogr.* **2022**, *206*, 102829. [[CrossRef](#)]
25. Shu, Y.; Wang, J.; Xue, H.; Huang, R.; Chen, J.; Wang, D.; Wang, Q.; Xie, Q.; Wang, W. Deep-current intraseasonal variability interpreted as topographic Rossby waves and deep eddies in the Xisha Islands of the South China Sea. *J. Phys. Oceanogr.* **2022**, *52*, 1415–1430. [[CrossRef](#)]
26. Isoguchi, O.; Kawamura, H. MJO-related summer cooling and phytoplankton blooms in the South China Sea in recent years. *Geophys. Res. Lett.* **2006**, *33*, L16615. [[CrossRef](#)]
27. Xie, Q.; Wu, X.; Yuan, W.; Wang, D.; Xie, S.-P. Life cycle of intraseasonal oscillation of summer SST in the western South China Sea. *Acta Oceanol. Sin.* **2007**, *26*, 1–8.
28. Xie, S.-P.; Chang, C.-H.; Xie, Q.; Wang, D. Intraseasonal variability in the summer South China Sea: Wind jet, cold filament, and recirculations. *J. Geophys. Res.* **2007**, *112*, C10008. [[CrossRef](#)]
29. Liu, F.; Tang, S. A double-peak intraseasonal pattern in the chlorophyll concentration associated with summer upwelling and mesoscale eddies in the western South China Sea. *J. Geophys. Res. Ocean.* **2022**, *127*, e2021JC017402. [[CrossRef](#)]
30. Herrmann, M.; To Duy, T.; Estournel, C. Intraseasonal variability of the South Vietnam upwelling, South China Sea: Influence of atmospheric forcing and ocean intrinsic variability. *Ocean Sci.* **2023**, *19*, 453–467. [[CrossRef](#)]
31. Roxy, M.; Tanimoto, Y. Influence of sea surface temperature on the intraseasonal variability of the South China Sea summer monsoon. *Clim. Dyn.* **2011**, *39*, 1209–1218. [[CrossRef](#)]
32. Wang, G.H.; Ling, Z.; Wu, R.; Chen, C. Impacts of the Madden–Julian Oscillation on the summer South China Sea ocean circulation and temperature. *J. Clim.* **2013**, *26*, 8084–8096. [[CrossRef](#)]
33. Jan, S.; Chang, M.H.; Yang, Y.J.; Sui, C.H.; Cheng, Y.H.; Yeh, Y.Y.; Lee, C.W. Mooring observed intraseasonal oscillations in the central South China Sea during summer monsoon season. *Sci. Rep.* **2021**, *11*, 13685. [[CrossRef](#)] [[PubMed](#)]
34. Ricciardulli, L.; Wentz, F.J.; Smith, D.K. *Remote Sensing Systems QuikSCAT Ku-2011 Weekly Ocean Vector Winds on 0.25 Deg Grid; Version 4*; Remote Sensing Systems: Santa Rosa, CA, USA, 2011.
35. Wentz, F.J.; Gentemann, C.; Hilburn, K.A. *Remote Sensing Systems TRMM TMI Weekly Environmental Suite on 0.25 Deg Grid; Version 7.1*; Remote Sensing Systems: Santa Rosa, CA, USA, 2015.
36. Le Traon, P.Y.; Dibarboure, G. Mesoscale mapping capabilities of multi-satellite altimeter missions. *J. Atmos. Ocean. Technol.* **1999**, *16*, 1208–1223. [[CrossRef](#)]
37. Cai, S.; Long, X.; Wu, R.; Wang, S. Geographical and monthly variability of the first baroclinic Rossby radius of deformation in the South China Sea. *J. Mar. Syst.* **2008**, *74*, 711–720. [[CrossRef](#)]
38. Locarnini, R.A.; Mishonov, A.V.; Antonov, J.I.; Boyer, T.P.; Garcia, H.E.; Baranova, O.K.; Zweng, M.M.; Johnson, D.R. *World Ocean Atlas 2009, Volume 1: Temperature*; Levitus, S., Ed.; NOAA Atlas NESDIS 68; U.S. Government Printing Office: Washington, DC, USA, 2010; 184p. Available online: <https://iridl.ldeo.columbia.edu/SOURCES/NOAA/NODC/WOA09/> (accessed on 20 February 2017).
39. Antonov, J.I.; Seidov, D.; Boyer, T.P.; Locarnini, R.A.; Mishonov, A.V.; Garcia, H.E.; Baranova, O.K.; Zweng, M.M.; Johnson, D.R. *World Ocean Atlas 2009, Volume 2: Salinity*; Levitus, S., Ed.; NOAA Atlas NESDIS 69; U.S. Government Printing Office: Washington, DC, USA, 2010; 184p. Available online: <https://iridl.ldeo.columbia.edu/SOURCES/NOAA/NODC/WOA09/> (accessed on 20 February 2017).
40. Wilkin, J.L.; Zhang, W.G. Modes of mesoscale sea surface height and temperature variability in the East Australian current. *J. Geophys. Res.* **2007**, *112*, C01013. [[CrossRef](#)]
41. Lin, H.; Thompson, K.R.; Hu, J. A frequency-dependent description of propagating sea level signals in the Kuroshio Extension region. *J. Phys. Oceanogr.* **2014**, *44*, 1614–1635. [[CrossRef](#)]
42. Bretherton, C.S.; Widmann, M.; Dymnikov, V.P.; Wallace, J.M.; Bladé, I. The effective number of spatial degrees of freedom of a time-varying field. *J. Clim.* **1999**, *12*, 1990–2009. [[CrossRef](#)]
43. Morimoto, A. Evaluation of tidal error in altimetry data in the Asian marginal seas. *J. Oceanogr.* **2009**, *65*, 477–485. [[CrossRef](#)]
44. Wang, D.; Zhuang, W.; Xie, S.-P.; Hu, J.; Shu, Y.; Wu, R. Coastal upwelling in summer 2000 in the northeastern South China Sea. *J. Geophys. Res.* **2012**, *117*, C04009. [[CrossRef](#)]
45. Lin, X.; Yang, J.; Wu, D.; Zhai, P. Explaining the global distribution of peak-spectrum variability of sea surface height. *Geophys. Res. Lett.* **2008**, *35*, L14602. [[CrossRef](#)]
46. Vialard, J.; Shenoi, S.S.C.; McCreary, J.P.; Shankar, D.; Durand, F.; Fernando, V.; Shetye, S.R. Intraseasonal response of northern Indian Ocean coastal waveguide to the Madden-Julian Oscillation. *Geophys. Res. Lett.* **2009**, *36*, L14606. [[CrossRef](#)]
47. Chen, G.; Hou, Y.; Zhang, Q.; Chu, X. The eddy pair off eastern Vietnam: Interannual variability and impact on thermohaline structure. *Cont. Shelf Res.* **2010**, *30*, 715–723. [[CrossRef](#)]

-
48. Hu, J.; Gan, J.; Sun, Z.; Zhu, J.; Dai, M. Observed three-dimensional structure of a cold eddy in the southwestern South China Sea. *J. Geophys. Res.* **2011**, *116*, C05016. [[CrossRef](#)]
 49. Vinayachandran, P.N.; Neema, C.P.; Mathew, S.; Remya, R. Mechanisms of summer intraseasonal sea surface temperature oscillations in the Bay of Bengal. *J. Geophys. Res.* **2012**, *117*, C01005. [[CrossRef](#)]

Disclaimer/Publisher's Note: The statements, opinions and data contained in all publications are solely those of the individual author(s) and contributor(s) and not of MDPI and/or the editor(s). MDPI and/or the editor(s) disclaim responsibility for any injury to people or property resulting from any ideas, methods, instructions or products referred to in the content.